Contents lists available at ScienceDirect

Arabian Journal of Chemistry

journal homepage: www.ksu.edu.sa

Lithium leach residue synthesis process of high crystallinity hydroxysodalite, NaX, NaA zeolites and solidification and migration of potentially toxic elements

Zongli Wang [a,b,c,d], Xianli Luo [b], Xiaojun Zheng [a,c,d], Ming Chen [a,c,d,*], Haifeng Guo [b], Qi Li [a,c,d]

[a] School of Resources and Environmental Engineering, Jiangxi University of Science and Technology, Ganzhou 341000, Jiangxi, China
[b] College of Materials and Chemical Engineering, Pingxiang University, Pingxiang 337055, Jiangxi, China
[c] Cooperative Innovation Center Jointly Established By the Ministry and the Ministry of Rare Earth Resources Development and Utilization, Ganzhou 341000, Jiangxi, China
[d] Jiangxi Provincial Key Laboratory of Environmental Pollution Prevention and Control in Mining and Metallurgy, Ganzhou 341000, Jiangxi, China

ARTICLE INFO

Keywords:
Lithium leach residue
Zeolite
Toxic elements
Migrate
Environmental Response

ABSTRACT

Converting lithium leach residue (LLR) into zeolite can reduce environmental impacts while also producing high value-added products. However, the synthesis of zeolites by LLR under alkali fusion may result in the solidification and migration of potentially toxic elements with secondary environmental impacts. Systematic research into this subject is rare in the open literature and the mobility of toxic elements from LLR derived zeolites is yet to be understood. In this paper, we have investigated the highly crystalline synthesis of hydroxy sodalite, X-type zeolite (NaX), and A-type zeolite (NaA) without stencil agent and crystal species, which can be achieved by modulating the alkali fusion temperature, all three zeolites have greater than 90 % conversion of the major elements aluminum and silicon. Meanwhile, the leachability of thallium (Tl), beryllium (Be), and potentially toxic elements (lead (Pb), mercury (Hg), cadmium (Cd), chromium (Cr), arsenic (As), barium (Ba), copper (Cu), nickel (Ni), cobalt (Co), zinc (Zn)) was monitored by pH-dependent leaching test for LLR and three kinds of synthesized zeolites according to the Chinese standard and the emission of toxic elements during the synthesis process was analyzed, to investigate the migration and quantify the distribution of the toxic elements in the LLR to the product zeolites and the cleaning wastewater. The migration efficiency of potentially toxic elements from LLR to the product zeolite and cleaning wastewater was explored. It was found that most of the toxic elements Tl, Be and potentially toxic elements were solidified in the structure of the zeolites by ion exchange (solidification rate $>$ 90 %), and a small portion flowed into the cleaning wastewater. Although there are toxic elements solidified in the structure, there is no significant leaching under various pH conditions, which is in line with the Chinese standard (GB/T 5085.3–2007). Therefore, it is considered that LLR realizes environmentally friendly zeolite production and does not cause secondary pollution to the environment. This work demonstrates great potential for green recycling of LLR from the lithium extraction process and introduces an environmentally friendly slag treatment technology.

1. Introduction

Lithium enjoys the reputation as “energy metal”, “aerospace alloy”, “white petroleum”, “the 21st century, the most potential metal” and so on (Kesler et al., 2012, Roy et al., 2023) is a high-end material necessary for high-tech emerging industries. However, utilizing lithium mica to prepare lithium carbonate results in a considerable amount of solid residue, known as lithium leaching (LLR), typically, 30–40 t of LLR are created for every 1 t of lithium salt (Li and Huang, 2020, Lv et al., 2022). As per China Nonferrous Metals Industry Association, China produced 0.125 million tons of Li-carbonate in 2018, which resulted in the 1 million tons discharge of LLR as waste (Sun et al., 2017). According to the properties of lithium mica, lithium(Li) is a companion element with thallium (Tl), beryllium (Be), etc. (Xu et al., 2023), so lithium mica may

* Corresponding author at: School of Resources and Environmental Engineering, Jiangxi University of Science and Technology, Ganzhou 341000, Jiangxi, China.
E-mail addresses: ZongliWang16@163.com (Z. Wang), Lxl2639659027@163.com (X. Luo), 2361781397@qq.com (X. Zheng), jxlgcm@163.com (M. Chen), guohaifeng720@163.com (H. Guo), liqibnu@foxmail.com (Q. Li).

https://doi.org/10.1016/j.arabjc.2024.105871
Received 9 April 2024; Accepted 10 June 2024
Available online 11 June 2024

contain Tl and Be. Also, lithium mica may contain potentially toxic elements such as lead (Pb), mercury (Hg), cadmium (Cd), chromium (Cr), arsenic (As), barium (Ba), copper (Cu), nickel (Ni,), cobalt (Co), zinc (Zn) (Zheng et al., 2024). Tl is one of the trace toxic elements (Wei et al., 2020) with greater acute and chronic toxic effects than other elements (e.g., Hg, Pb, or Cd) in most organisms (Aguilar-Carrillo et al., 2018), and it is classified as one of the 13 Priority Pollutants by the Environmental Protection Agency (EPA) (U.S. EPA, 2014). Be has been classified as a carcinogenic since Beryllium has been classified as a carcinogenic heavy metal since 1987. Therefore, the use of open piles for treatment and disposal of LLR creates a problem of potential contaminant impacts on groundwater, surface water, and soil (Dong et al., 2021). The problem of proper utilization and disposal of LLR solid waste has become a bottleneck restricting the development of the lithium salt industry.

At present, LLR is currently utilized in construction concrete due to its good adsorption (specific surface area 430–440 m^2/kg) (He et al., 2017), chemical exciter effect, and filling effect with volcanic ash reaction (He et al., 2017, Chen et al., 2018), but at a low admixture level. From the point of view of cleaner production and high added value, LLR is a waste that needs immediate attention and proper and effective disposal, while from the point of view of waste utilization, LLR is a resource to be fully utilized. LLR is rich in silica and aluminum phases and has the same composition as zeolite, the difference between the two being the difference in crystal structure, with zeolite having a well-defined crystal structure and LLR consisting of an amorphous structure (Kuang et al., 2015, Yiren et al., 2019). Due to these similarities, LLR has been recognized as an ideal raw material for zeolite synthesis. X-type (NaX) zeolite, and A-type (NaA) zeolite are widely used in the chemical industry (Jain et al., 1990, He et al., 2019), water purification (Feng et al., 2018, Li et al., 2023, Li et al., 2024), gas purification (Kim et al., 2016, Muriithi et al., 2020, Zhao et al., 2024), energy and medicine and other emerging applications (Heard et al., 2019). Hydroxy sodalite (HS) is used in the chemical industry, such as the separation of small gas molecules (H_2, styrene, CO_2) (Wang et al., 2016, Zhai et al., 2019, Gordina et al., 2022). These zeolites have become one of the most important materials today. Therefore, it is feasible to convert LLR to zeolite, which not only has the potential to alleviate the waste disposal problem, but also has the potential to produce high-value products.

Two-step hydrothermal and melt-assisted methods are more feasible for industrial applications of zeolite preparation (Chen et al., 2023), enabling the preparation of zeolites with higher crystallinity without the need for templating agents and crystal seeds (Feng et al., 2018). The two-step alkali fusion method is in the presence of alkaline exciters, SiO_2 and Al_2O_3 interact and condense to form a white gel with silica-aluminate anions, and under heating prompts the gel to dissolve and increase in size, the ion concentration in the liquid phase increases, and hydrated anions rearrange to form nuclei, which grow to form zeolites (Bukhari et al., 2015, Sivalingam and Sen, 2018). That is, temperature induces the creation of different crystal nuclei and the formation of different zeolites (Palomo et al., 2014). Meanwhile, the migration of toxic elements may occur in LLR in the presence of alkaline exciters, as well as the solidification within the zeolite lattice, and the migration or solidification mechanism and whether the zeolite produces secondary contamination in environmental and industrial applications have not yet been investigated. This will be the key to the high-value-added resource utilization of LLR-prepared zeolites.

Therefore, a two-step alkali fusion method was used in this study to realize the green conversion of LLR to HS, NaX, and NaA zeolites by controlling the change of alkali fusion temperature. The three zeolites were characterized by powder X-ray diffraction (XRD), scanning electron microscopy (SEM), transmission electron microscopy (TEM), X-ray fluorescence (XRF), Fourier transform infrared spectroscopy (FTIR), and Brunner-Emmett-Teller (BET) surface analysis, and the conversion ratios of major elements were calculated. In addition, the LLR-generated zeolite processes and products were quantitatively analyzed for harmful element migration and leachability to explore the curing mechanism.

Table 1
Chemical composition of LLR.

	SiO_2	Al_2O_3	Na_2O	K_2O	CaO	Fe_2O_3	other
Chemical composition content (%)	50.87	29.6	4.108	1.37	7.378	3.056	3.618

The technical feasibility and environmental response of LLR for the preparation of high value-added zeolite products were verified.

2. Experimental

2.1. Materials

The LLR used in this experiment is the slag of lithium mica leached by the sulfate method, which is sourced from a lithium carbonate producer in Jiangxi Province, China. The LLR is a powder that has a water content of 2.51 % after natural drying. Its pH is 8.2 with a liquid-to-solid ratio of 2.5:1, a specific surface area of 420 m^2/kg, and a cation exchange rate of 0.08 cmol/kg^{-1}. The chemical composition of LLR is listed in Table 1. Its Si/Al≦2 can be used to make X-type and A-type zeolites with low Si/Al ratios (Huang et al., 2023).

2.2. Preparation and analysis of zeolites

HS, NaX, and NaA zeolites were green synthesized by a two-step alkali fusion method without adding any templating agent or crystal species. Which are divided into three key steps: pretreatment, alkali fusion, and crystallization. **Pretreatment**: The LLR was placed in ultrapure water (>18.2 MΩ) at a liquid–solid ratio of 10:1 and then shaken in a water bath shaker (10 ± 2r/min) for 5 min at room temperature (23 ± 2 °C), retaining cleaning water 1. Without acid washing to reduce leaching and emission of toxic elements. **Alkali fusion**: The alkali fusing agents NaOH and LLR were added in the crucible according to the alkali/silicon molar ratio (2 ~ 2.2):1, and the reaction was carried out in a muffle furnace according to different alkali fusing temperatures (300–800 °C) for 6 h, and the light blue crystals were obtained when the reaction was cooled down to room temperature after completion. **Crystallization**: In an auto-clave, light blue crystals, and deionized water were added at a mass ratio of 1: (11–13), and the product was crystallized at 90 °C for 8 h. The product was washed (retaining the washing water 2) and dried to obtain zeolite. In all processes, no solid waste was discharged and the wash water was retained for analyzing the migration of the target heavy metal elements. NaOH is a chemically pure grade.

The conversion *Ci* of the two major elements silicon and aluminum is an important parameter indicating the efficiency of LLR utilization, which can be calculated from Eq. (1):

$$Ci\% = \frac{Mz \cdot Xzi}{M_{LR} \cdot Xi} \times 100\% \quad (1)$$

where i denotes the element of interest. M_{LR} (kg), the mass of LLR. Xi (%), the proportion of elemental content in LLR. Mz (kg), the mass of zeolite. Xzi (%), the proportion of element of interest i in zeolite.

The relative crystallinity of zeolites was calculated by the "peak fitting" algorithm method using the JADE 6.5 software and the calculated equation was shown in Eq. (2):

$$Relativecrstallinity = \frac{\sum S_{zerolites}}{\sum S_{standard}} \times 100\% \quad (2)$$

where *Szeolites* was the area of all the HS, NaA, and NaX zeolite characteristic peaks (13.9 °, 24.4 °, 29.4 °, 34.4 ° 2θ for HS; 6.1 °, 16.9 °, 23.3°, 26.7° 2θ for NaX and 7.30 °, 10.3 °, 24.02°, 29.98° 2θ for NaA respectively) in the product. The standard is the sum of the intensities

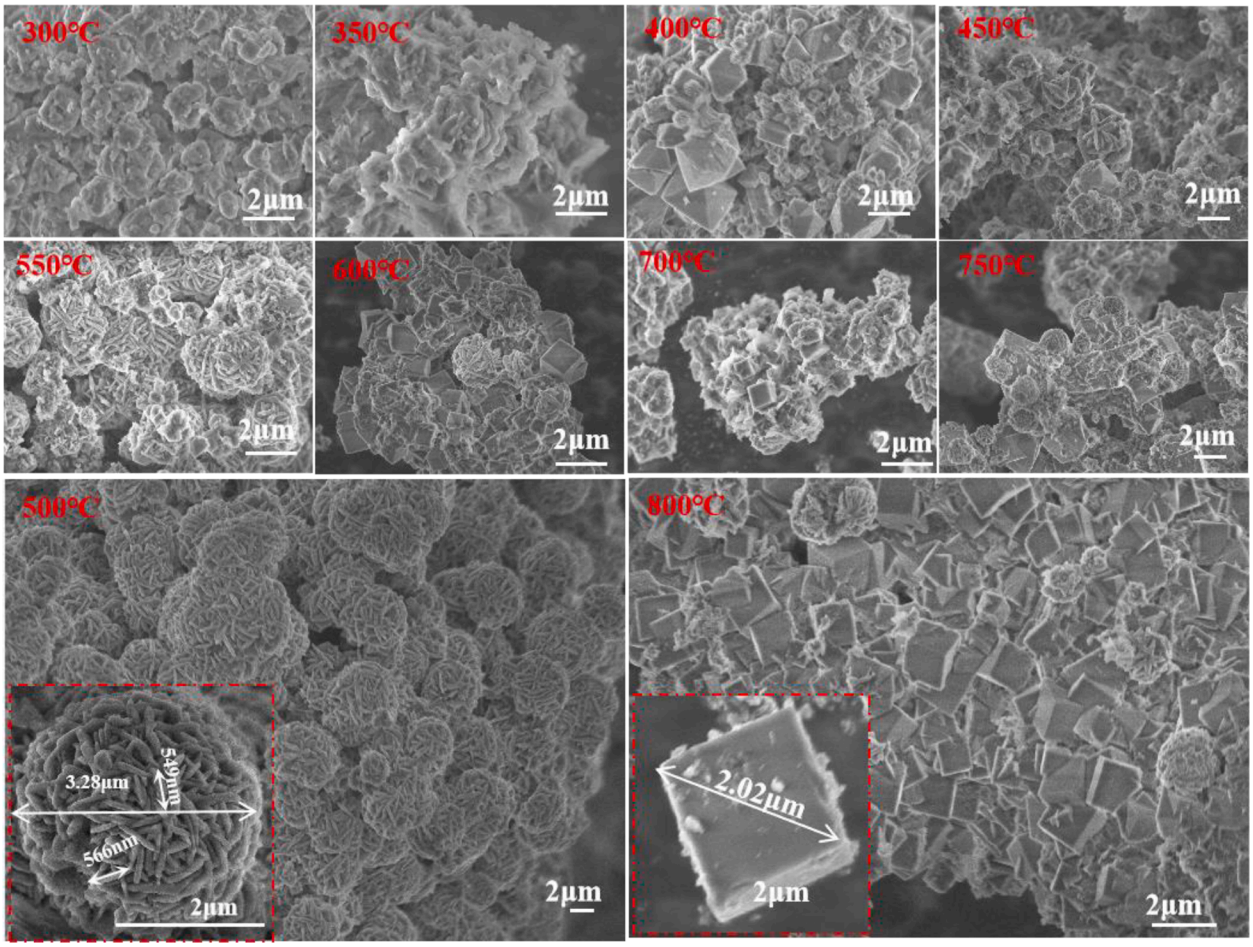

Fig. 1. Typical SEM variation images of zeolite samples synthesized with different alkali fusion temperatures(300 °C -800 °C), where NaX zeolite was synthesized at 400 °C, HS at 500 °C, and NaA zeolite at 800 °C.

corresponding to a change in the mass fraction of crystalline zeolite versus a change in the mass fraction of crystalline zeolite judged to be a pure sample (i.e., not changing over a prolonged period of time during the crystallization process), calculated by normalizing the sum of the intensities of the four zeolite-strong peaks.

2.3. Measurement and characterization

The microscopic morphology of the samples was analyzed by cold field emission scanning electron microscopy (SEM, Hitachi 8010, Japan). The transmission electron micrographs (TEMs) and high TEMs (HRTEMs) of samples were measured on a microscope (TEM, FEI, tecnaiF20, USA) operating with 200 kV equipped with an ORIUS Gatan Camera. The samples were physically analyzed by X-ray diffraction analysis (XRD, Bruker D8, Germany), with Cu target, 40 mA tube current, 40 kV tube voltage, continuous scanning, and a slit system with a DS (emission slit) of 1/2°, an SS (scattering prevention slit) of 0.04 rad, and an AAS (acceptance slit) of 5.5 mm. The scanning range was $2\theta = 5°\sim80°$. The chemical composition of the LLR and zeolite products was determined by X-ray fluorescence (XRF, Zetium-DY3858, NLD). The samples were analyzed by infrared absorption spectrometry (FITR, Bruker TENSOR27, Germany) with a scanning range of 4000 ~ 500 cm^{-1} and KBr flake method. Nitrogen sorption instrument (Micromeritics, ASAP2420, USA) was used to detect the Brunauer-Emmet-Teller (BET) specific surface area. The pore size distribution was plotted based on the Horvath-Kawazoe (HK) method.

2.4. Metal leaching and heavy metal migration test

The environmental risk of leaching of toxic elements from LLR and product zeolites was analyzed by pH-dependent leaching tests. Tl^+ is soluble and more soluble in the range of pH 0 to 13, and TlOH precipitation is formed at pH > 13 (Li et al., 2021). Therefore, leachants with pH values of 1, 3.21, and 5 were prepared with reference to the H_2SO_4-HNO_3 method in China Solid Waste Leaching Methods (HJ/T299-2007) (in which 3.21 was set as the leaching pH according to the toxic leaching requirement for solid waste of pH = 3.2 ± 0.05 as specified in HJ/T299-2007). Preparation of leachate with pH 12 and 13 using NaOH method. Neutral conditions and natural weak acidic conditions were simulated using deionized water and carbonated water, with pH 7 and 6, respectively.

The product was dried twice at 105 °C to an error of <±1% (determination of water content), and according to the water content of the sample, the product was put into the extracting agent at a liquid–solid ratio of 10:1 (L/kg), and then shaken in a water-bath constant temperature oscillator (30 ± 2r/min) at room temperature (23 ± 2 °C) for 18 ± 2 h. The upper layer of the supernatant was passed through a micropore membrane with a pore size of 0.45 um, and then the product was adjusted to a pH < 2 with dilute nitric acid, and stored at 4 °C for measurement. The pH was determined by a pH meter, and determination of toxic elements in solutions was carried out by inductively coupled plasma mass spectrometry (ICP-MS, PinAAcle 900H). The containers used for the tests were immersed in (1 + 2) HNO_3 solution for more than 24 h before use. The test samples were 3, parallel samples and analyzed using national standard solutions to control the working curve.

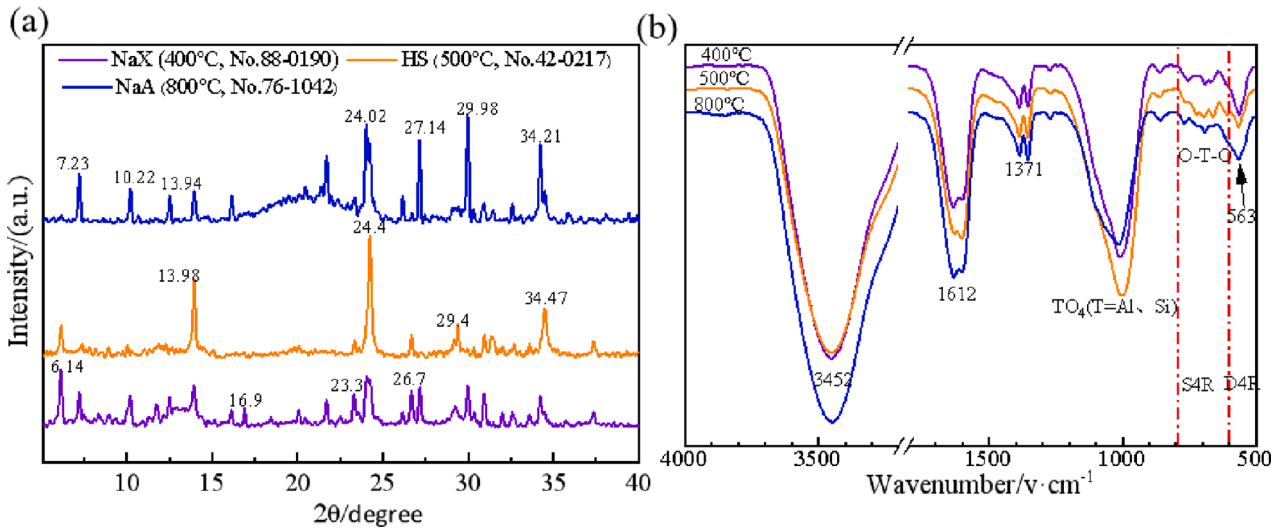

Fig. 2. XRD images (a) and FTIR images (b) of zeolites synthesized at different alkali fusion temperatures, where 400 °C is NaX zeolite, 500 °C is HS, 800 °C is NaA zeolite.

The reagents used were of analytical grade: 98 % (w/w) H_2SO_4, 65 % (w/w) HNO_3. All standard solutions were prepared in polypropylene vials with deionized water (> 18.2 MΩ) and 1 % (diluted by volume) nitric acid (Senila et al., 2022). 1 % ammonium chloride (NH_4Cl) was added to all samples and standard solutions to eliminate interference from iron ions.

At the same time, the migration of toxic elements in the effluent during the synthesis process was tracked, and the toxic elements content was measured using ICP-MS.

3. Results and discussion

3.1. Three kinds of zeolite were synthesized under temperature control

3.1.1. Changes in structure and morphology at different alkali melting temperatures

The structure and morphology of the zeolite products at alkali melting temperatures (300–800 °C) were characterized using XRD and SEM, respectively, to monitor the type and quality of the products. Fig. 1 shows the change in the zeolite phase with increasing alkali fusion temperature. As the alkali melting temperature increases, the mullite in LLR undergoes a phase change reaction with alkali, and the original SiO_2 and Al_2O_3 hydrated cations at low temperatures come into contact with each other under the action of the alkali melt and condense into a white gel-like silica-aluminum anion (350 °C), and the elevated temperature induces an increase in the solubility of the gels, an increase in the concentration of liquid-phase silica-aluminate anions, and the hydrated anions undergo a renewed coordination polycondensation to form zeolite units, and crystallization and nucleation. When the alkali melting temperature is controlled at about 400 °C, the hydrated anions undergo coordination condensation to nucleate into particles and grow around the center to form an octahedral three-dimensional shape, which is the characteristic structural shape of NaX zeolites (Novembre et al., 2018, Muriithi et al., 2020). When the temperature was gradually increased to 500 °C, the hydrated anionic skeleton growing around the center was rearranged to form β-cage HS. Whose morphology showed alternating layers of molecular sieves from spherical clusters arranged into plate-like structures, with the length of molecular sieve crystals ranging from 500 to 600 nm and the width from 66 to 99 nm, which was consistent with the results of the HS prepared from part of the fly ash (Muriithi et al., 2020). When the temperature was further increased, the striated molecular sieves on the spherical surface dissolved (550 °C), became finer and shorter (600 °C), and formed a three-dimensional skeletal structure of β-cages connected by a double 4-membered ring (D4R) in the center of the crystalline cells, which gradually formed the cubic-structured NaA zeolite (700 °C) (Bukhari et al., 2015, Feng et al., 2018, Cao et al., 2020, Mamaghani et al., 2023).

Fig. 2(a) shows the XRD patterns of the three synthesized zeolites. At the alkali melting temperature of 400 °C, a characteristic diffraction peak (d110 = 0. 633 nm) appeared in the XRD pattern, indicating that the system has reached the alkalinity required for the growth of zeolite, and the environment of the system began to be suitable for the growth of zeolite, and the diffraction peaks of the single-phase NaX zeolite appeared at 6 0.1°, 16.9°, 23.3°, and 26.7°, and the relative crystallinity was 51.6 %, respectively (Novembre et al., 2018). The characteristic diffraction peaks of the NaX zeolite weakened and shifted towards 13.9°, 24.4° and 34.47° as the alkali melting temperature was gradually increased, and the HS was formed at 500 °C (Prokof'ev and Gordina, 2014), when the relative crystallinity was 95. 2 %. As the temperature increases to 800 °C, the HS diffraction peaks shift to 7°, 10°, 13°, 24°, 27°, and 30°, which are categorized as typical characteristic diffraction patterns of A-type zeolites (Feng et al., 2018). Relative crystallinity of 78 %.

The above-mentioned XRD data are confirmed by the FTIR spectroscopic data. Fig. 2(b) shows the FTIR spectra of the three zeolites. The stretching and bending vibration peaks of adsorbed and zeolite water in the samples are shown at 3452 and 1612 cm^{-1}, the bands in the range of 1047–960 cm^{-1} are attributed to the antisymmetric stretching vibration of TO_4 (T = Si or Al) (Criado et al., 2005, Yang et al., 2019, Lv et al., 2022). In addition to this, in the range 600–500 cm^{-1} are the absorption bands of double 4-ring (D4R), through which the β-cage is connected in the zeolite framework. 565 cm^{-1} is the characteristic peak of double 4-membered ring (D4R) in a typical A zeolite structure, and D4R is one of the most dominant secondary structural units (SBU) in the NaA zeolite structure, and the intensity of its absorption peak can be used as an important symbol to judge the growth of NaA zeolite (Prokof'ev and Gordina, 2014). All samples embodied absorption bands in the range of 800–600 cm^{-1}, which are zeolite species bonding bands, symmetric telescopic vibration peaks of T-O-T in the zeolite structure (Prokof'ev and Gordina, 2014), which corresponds to the 6-ring structure of the β-cage of the simple 4-ring, which is a typical feature of the SOD structure. Compared with the FTIR spectra of the zeolite product (HS) at 500 °C, the peak strength at 1016 cm^{-1} of the zeolite product (NaX) at 400 °C, zeolite product (NaA) at 800 °C is significantly lower, which further suggests that there is more alternating condensation of Si-O and Al-O bonds in the HS, and a greater amount of aluminum ions penetrate

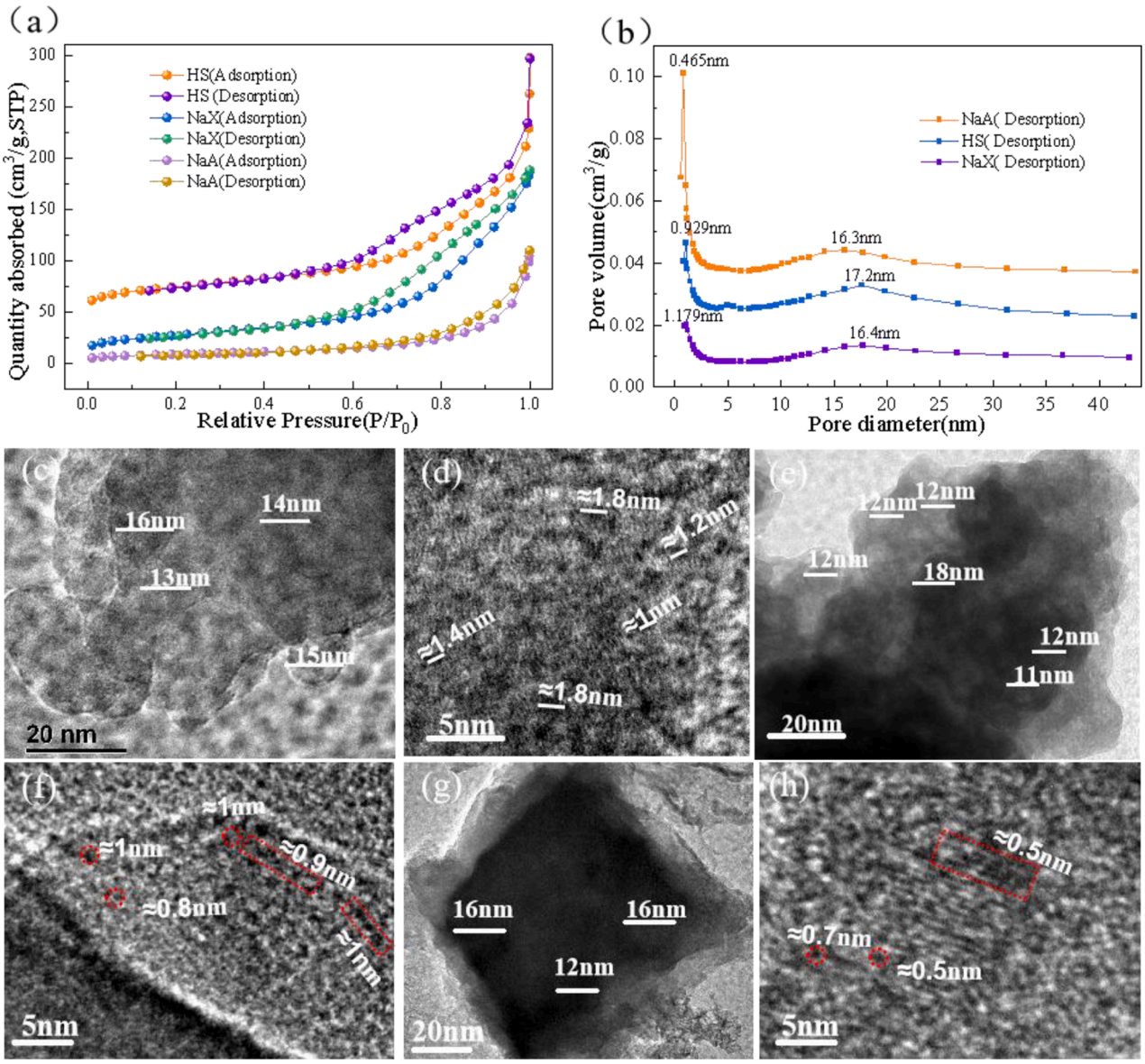

Fig. 3. TEM images of zeolites (c, d = NaX, e, f = HS g, h = NaA) and nitrogen adsorption–desorption isotherms(a) and HK pore size distribution curve of zeolite(b).

into the TO4 tetrahedra (Palomo et al., 2014; Liu et al. 2018), which suggests that more zeolites were formed in the product at 500 °C, which is consistent with the results of scanning electron microscopy analysis.

3.1.2. *BET surface area*

The three zeolites were further characterized by N_2-BET and their adsorption isotherms and HK pore size distribution curves are shown in Fig. 3. The obtained isotherms indicate that all three zeolites are a microporous and mesoporous material, which can be categorized as class IV isotherms. It takes a long time to perform multilayer filling in the adsorption isotherm (region between 0.1 and 0.6P/P_0), while delayed condensation is observed at a P/P_0 value of about 0.9. The sharp capillary condensation step indicates a narrower pore size distribution for the three zeolites. Among the three zeolites, HS has the largest specific surface area of 181.1987 m^2 /g and NaX has a specific surface area of 95.8473 m^2 /g, both of which are of the same grade as reported zeolites(Chen et al., 2012, Muriithi et al., 2020, Mamaghani et al., 2023). The pore sizes of HS are about 9 Å, those of NaX zeolite are about 12 Å, and those of NaA zeolite are about 4 Å, which are consistent with the TEM result of Fig. 3 (c, d, e, f, g, h). The high-resolution images show that the crystal sizes of the three zeolites range from 9 to 18 nm. However, the pore-filling effect of NaA zeolite structure was found to be small, with a total surface area of only 41.38 m^2 /g, a microporous area of 11.93 m^2 /g, and an external surface area of 29.19 m^2 /g, which is of the same order of magnitude as that of the previously reported NaA zeolite (Jiang et al., 2015), which has a total surface area of 41.6 m^2 /g. The reason for the small specific surface area of NaA zeolite may be related to the finding by that in many of the small-pore zeolites where a molecular trapdoor effect occurs, where the center of the eight-membered ring (i.e., the entry point of the N_2 molecule) in NaA (Feng et al., 2018, Cheng et al., 2024) is partially blocked by its cations at 77 K, resulting in almost no measurable BET surface area.

Table 2
Conversion rates of major elements Si and Al in zeolite.

Elements	LLR	NaX	HS	NaA
Si Mass ratio, %	~23.74	~24.46	~25.78	~28.78
Si conversion rate, %	/	91.3	93.6	96.5
Al Mass ratio, %	~15.4	~15.87	~16.72	~18.67
Al conversion rate, %	/	96.3	97.6	98.2

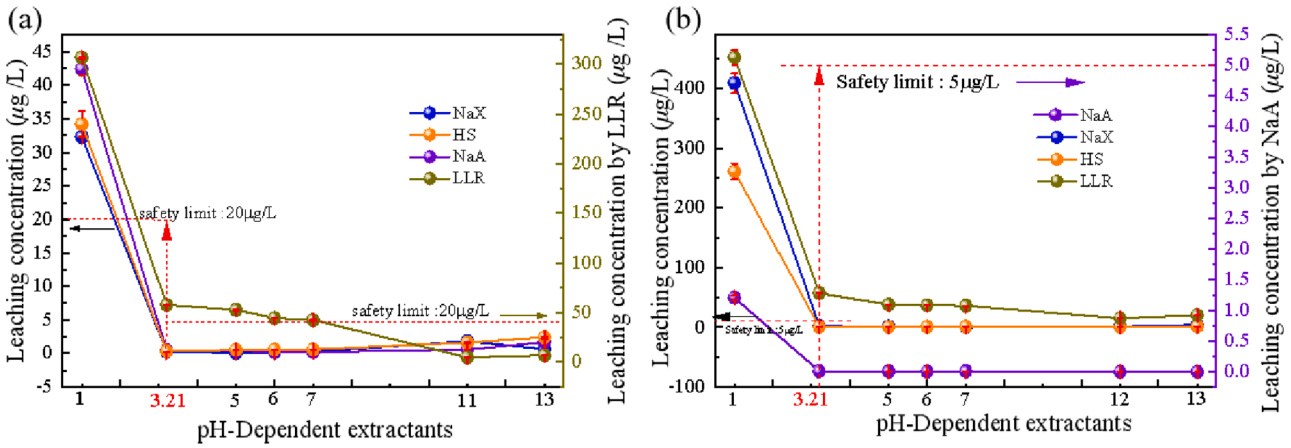

Fig. 4. Leaching concentration of Be(a), Tl(b) at pH = 1, 3.21, 5, 6, 7, 11, 13 for HS, NaX zeolite, NaA zeolite, LLR, where safely limit Refer to the Chinese standard (GB/T 5085.3–2007).

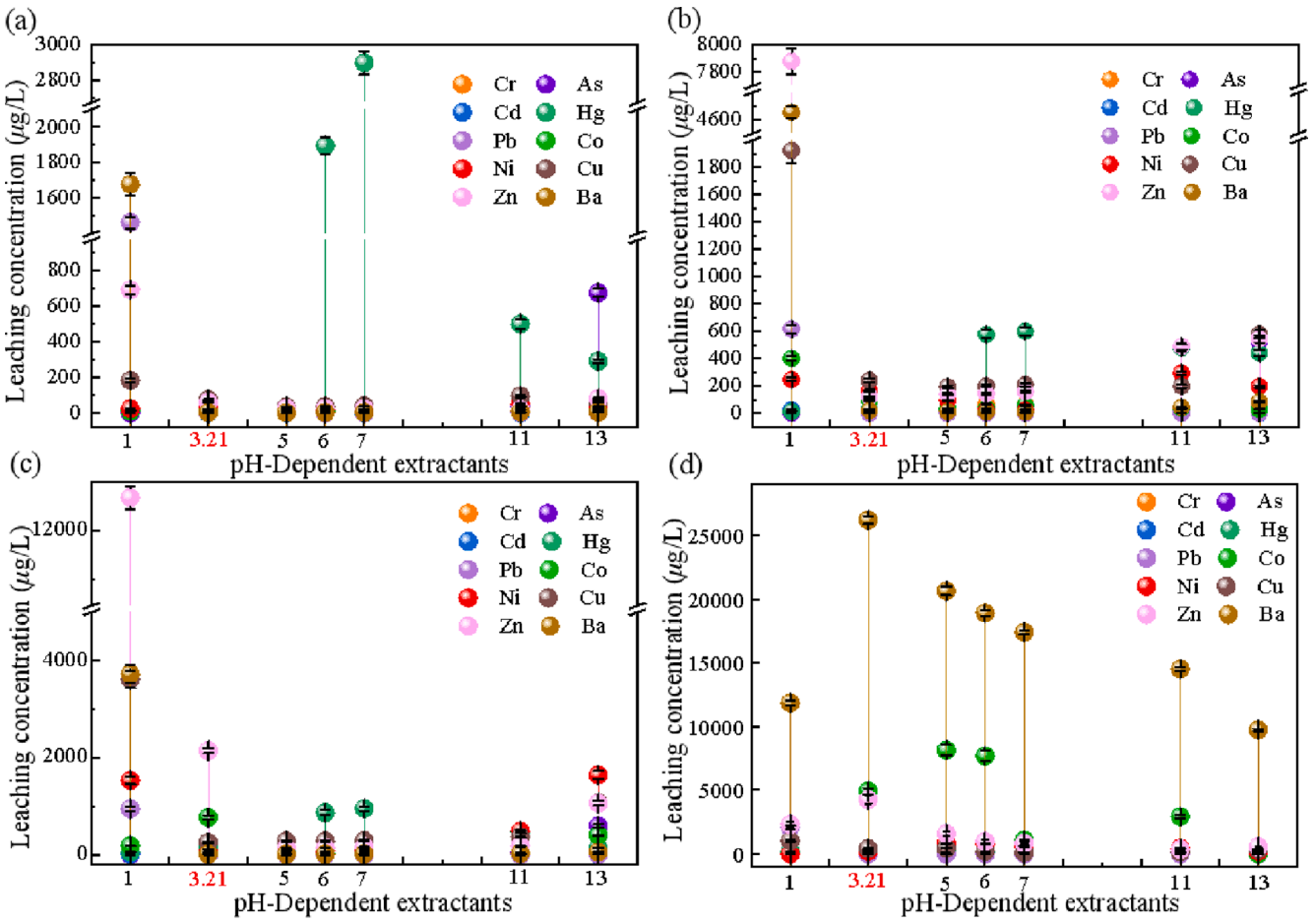

Fig. 5. Leaching concentration of potentially toxic elements of HS (a), NaX (b), NaA (c), LLR(d) at pH = 1, 3.21, 5, 6, 7, 11, 13.

3.1.3. Conversion rate of major elements Si, Al

The conversion rates of Si and Al in this zeolite synthesis process are important indicators of the effectiveness of the LLR recycling process. By analyzing the Si and Al elements in the three zeolite products, the conversion rates of Si and Al, the two main elements of the three zeolites (Table 2), were calculated to be greater than 90 % according to Equation (1), which demonstrates the high efficiency of the method of synthesizing lithium residue-based zeolites by the two-non-alkali fusion method. The significance of a high conversion rate is to ensure that the economy is maximized and secondary waste is minimized.

3.2. Migration of toxic elements

In the zeolite synthesis process and use, these toxic elements migrate and leach whether the secondary pollution of the environment is the focus of the product input engineering.

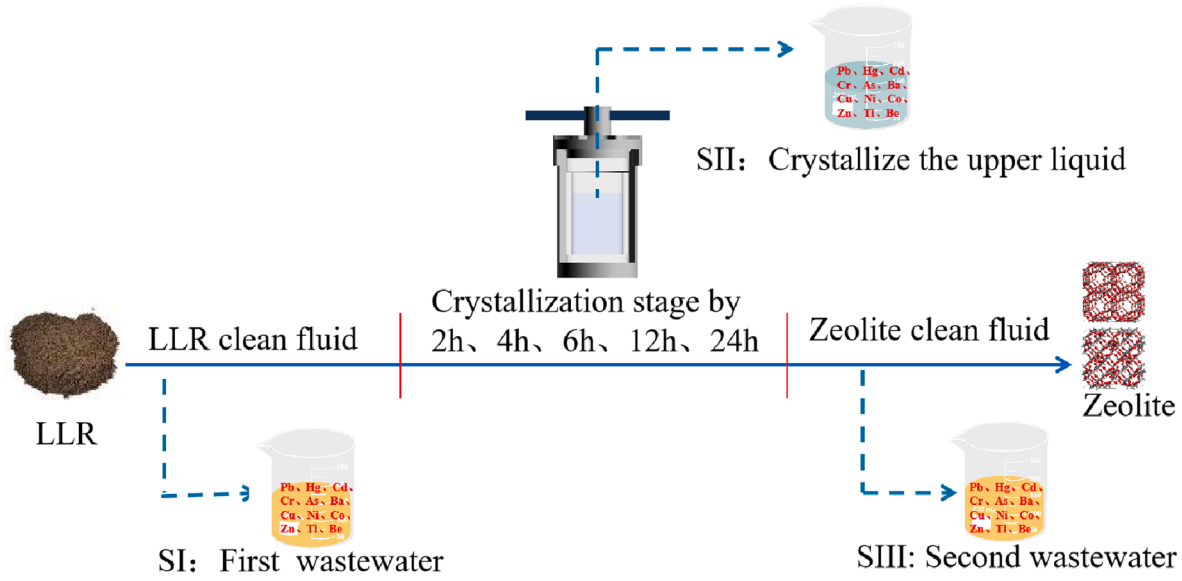

Fig. 6. An overview of toxic elements distribution and migration paths.

3.2.1. Leaching of toxic elements from zeolites

Consider the leaching risk of the main toxic elements Be, Tl, and the potentially toxic elements Pb, Hg, Cd, Cr, As, Ba, Cu, Ni, Co, Zn in the use of the product. The leaching risk at different concentrations was analyzed by pH-dependent experiments. And compared with the Chinese standard (GB/T 5085.3–2007) to determine whether there is a secondary environmental response hazard in the use of the three zeolite products.

As can be seen from Fig. 4, the Be concentration leaching from LLR at pH = 3.21 was as high as ~57.99 μg/L, which was 3 times the standard limit value of 20 μg/L. The Tl concentration was as high as ~57.59 μg/L, which was 11 times of the standard limit value of 5 μg/L. Which indicated that LLR was a hazardous waste. On the other hand, the three zeolites were lower than the standard limit value of leaching and did not show any hazardous characteristics, indicating that the zeolites prepared by alkali fusion of LLR can effectively avoid the leaching hazards of Be and Tl.

Meanwhile, the leaching concentration of toxic elements Tl in LLR was as high as ~451.07 μg/L, which exceeded the standard by 90 times. The leaching concentration of Tl in HS and NaX zeolite after alkali fusion was very low in all other pH gradients, except for Tl leaching concentration exceeding 50 times in concentrated acid at pH = 1. Especially, the NaA zeolite under alkali fusion at 800 °C was not leached under any pH condition, indicating that the toxic elements Tl were better encapsulated and blocked by ion exchange at the elevated alkali fusion temperature.

Fig. 5 shows the leaching of other potentially toxic elements under a pH gradient. It was found that the leaching concentrations of toxic elements (Pb, Hg, Cd, Cr, As, Ba, Cu, Co) were higher in LLR than in the zeolite product at all pH gradients. In contrast, Ni and Zn were leached at concentrations comparable to those of LLR, suggesting that conversion of LLR to zeolite can significantly reduce the risk of harmful toxicity. At pH = 3.21, the leaching concentrations of toxic elements from all three zeolites were below the standard limits, while Ba, Hg, and Co in LLR exceeded the standard limits, showing the characteristics of hazardous waste. Meanwhile, it can be found from Fig. 5 (a, b, c) that the leaching concentration of Hg is higher under the neutral leaching agent condition, and HS zeolite has the lowest leaching concentration for all types of toxic elements. Combined with the scanning electron microscope data, it is found that HS zeolite has the highest relative crystallinity because zeolite can encapsulate and block the toxic elements well, and with the increase in the relative crystallinity of zeolite in the samples, the leaching concentration of the samples for the toxic elements decreases (Bukhari et al., 2015).

In conclusion, the leaching concentration of toxic elements of zeolite prepared by the two-step alkali fusion method meets the Chinese GB/T 5085.3–2007 standard. The prepared HS has no secondary environmental risk reaction to the environment, the leaching rate is the lowest, and the relative crystallinity is more than 95 % under the condition of no templating agent and crystal seed, so it can realize the industrialized production and large-scale application.

3.2.2. Migration of toxic elements in production

The pH-dependent leaching experiments showed that among the three zeolite products, the leaching concentration of each toxic element in HS was the lowest, indicating that the toxic elements were best solidified in the HS. To further investigate the curing efficiency of toxic elements in zeolite and to analyze whether the zeolite production process will produce secondary environmental pollution, HS was used as an experimental object to analyze the heavy metal migration during the production process.

Fig. 6 shows the possible pathways of migration of various elements from the original LLR and the synthesized zeolite product in the production chain of zeolite. The zeolite synthesis process involves a hydrothermal treatment with a strongly alkaline solution at elevated temperatures, which breaks down the mullite and quartz hard crystalline phases in LLR, making Si and Al available for zeolite synthesis. At the same time, all other elements in the LLR are released and allowed to move (Feng et al., 2018).

Two steps of the experiment will produce waste liquids (Fig. 6 SI, SIII) to test the content of toxic elements in the effluent of the external environment. In addition, in the experiment there is an upper layer of clear liquid after crystallization in the auto-clave (Fig. 6 SII) (note that this part of the waste liquid is not dumped but goes directly to the next step of the drying experiments), and the content of toxic elements in the upper layer of the clear solution to verify the curing efficiency of toxic elements in zeolites.

It was found that the toxic elements content in the upper clear liquid changed with the change of crystallization time, so the crystallization time was set to 2 h, 4 h, 6 h, 12 h, and 24 h to examine the difference of cured toxic elements. The migration of toxic elements from LLR to zeolite was examined by analyzing the two waste steps as well as the upper clear liquid of the reactor to analyze the partitioning and quantitative distribution of these elements in the process wastewater and

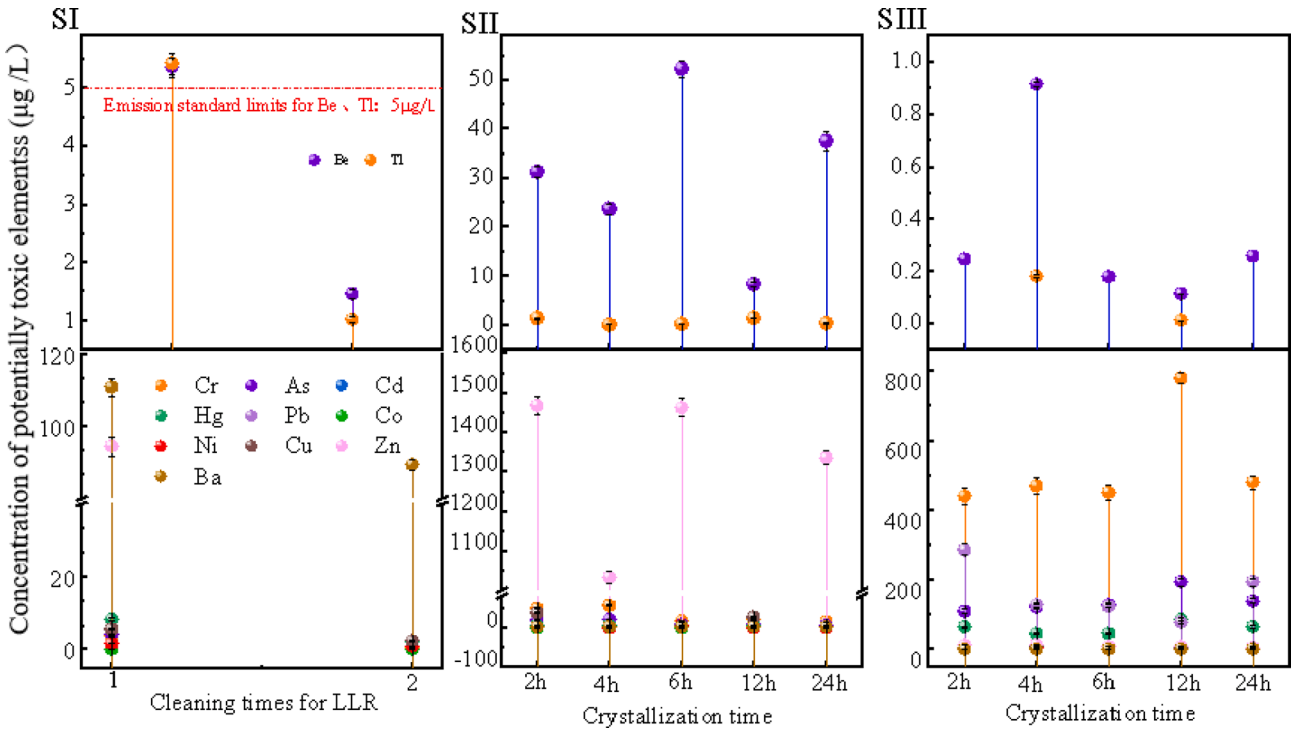

Fig. 7. Migration of toxic elements during the preparation process (where SI – LLR cleaning, SII – crystallization stage, SIII – zeolite product cleaning).

Table 3
Solidification rate of toxic elements in zeolite.

Toxic elements	Solidification rate, %	Toxic elements	Solidification rate, %
Be	~99.22	Pb	~92.56
Tl	~99.99	Co	~98.53
Cr	~90.9	Ni	~90.91
As	~82.97	Cu	~97.22
Hg	~93.1	Zn	~99.22
Cd	~99.99	Ba	~99.52

zeolite. In the following discussion, the concentration of the wastewater discharge is compared to the ceramic manufacturing emission standard limits to determine the environmental feasibility in the production step.

The LLR was cleaned twice with ultrapure water at a solid–liquid ratio of 1:20 (10 ± 2r/min for 5 min). From (Fig. 7 SI), it can be found that there will be precipitation of Be and Tl in the cleaning stage of the LLR, and the wastewater of the first cleaning exceeded the standard in a small amount of Be and Tl, and the content of Hg was ~ 8.174 μg /L, it satisfied the standard discharge limit of < 50 μg/L, and the rest of the toxic elements were lower than the standard limits (Pb ≤ 300 μg /L, Cd ≤ 70 μg/L, Cr ≤ 100 μg /L, As ≤ 500 μg /L). All kinds of toxic elements in the secondary cleaning wastewater meet the requirements of the emission standards, and some elements do not meet detection limits. After the completion of production, under the operating conditions of solid–liquid ratio of 1:20, the product zeolite was cleaned with ultrapure water (10 ± 2r/min, 5 min). From (Fig. 7 SIII), it can be found that Be, Tl, Cr, Zn, and As, leaching concentrations in the zeolite cleaning solution within 4 h of crystallization were relatively high, but could meet the limits of the emission standards.

In addition, we examined the content of toxic elements in the upper clear liquid within the auto-clave during the crystallization phase to determine the rate of solidification of toxic elements in the zeolite. From (Fig. 7 SII), it can be found that the toxic elements concentrations were higher than the SI and SIII stages at all crystallization times. Among them, the concentrations of Zn, Cr, Pb, As, and Be, were higher, with Zn maintained at ~1300 μg/L, Cr reaching a maximum value of 778.6 μg/L at 12 h of crystallization, and Pb reaching a maximum value of 286 μg/L at 2 h of crystallization. In the experiments, the solid–liquid in the reactor was directly reacted and dried, i.e., captured and immobilized in the zeolite structure, so the solidification rate of the toxic elements was calculated by comparing the SII concentration with the SIII concentration, as shown in Table 3.

The toxic elements are classified into three groups based on the solidification rate, the first group(I) includes Tl, Be, Cd, Cu, Zn, Co, and Ba whose solidification rate is close to 100 %. This is due to zeolite owning to its unique physicochemical and surface (charge) properties, amphoteric ligand capacity and hollow "nanoball" structure (Baldermann et al., 2018), the ability of such toxic elements to exchange with adsorption sites in zeolites is dependent on short-range order aluminosilicates for some toxic elements such as Cs^{+}, Ba^{2+}, Co^{2+}, Cu^{2+}, Sr^{2+}, and Zn^{2+}, with unique physicochemical and surface (charge) properties, amphiphilic ligand capabilities and hollow "nanopore" structures (Wu et al., 2018, Baldermann et al., 2020). The second group (II) consists of Pb, Hg, and Cr, are 2-sex elements (Inoue et al., 2017), with immobilization rates of about 90 %, while the solidification rate of this group of toxic elements increases with crystallization time. For example, about 8 % or so of Pb enters the alkaline wastewater after crystallization and drying by washing, and the presence of Pb in the waste can be attributed to the formation of soluble anionic hydroxyl complexes (Huang et al., 2004), such as $[Pb(OH)_4]^{2-}$ or $[PbO_2]^{2-}$ (Zeng et al., 2019), most of the amphiphilic Pb(II) in LLR may be solidified in the zeolite lattice by forming hydrated anions with Si^{2+} in the presence of NaOH. The multivalent cations in the above two groups, due to their low solubility in supercritical water at high pH, the toxic elements in the LLR can be captured by physical/chemical adsorption, ion-exchange and physical encapsulation during the formation of amorphous or crystalline silica-aluminate. The heavy metal ions are adsorbed or encapsulated in the zeolite skeleton, which has a high immobilization rate (Bukhari et al., 2015). The third group (III) is the quasi-metal of As (Calugaru et al., 2018), which has a fixation rate lower than 90 %. Which may be attributed to the general negative electronegativity of the zeolite skeleton and the dissolution of arsenate complexes (AsO_4^{3-}) in LLR under strongly alkaline conditions during the hydrothermal reaction, thus the

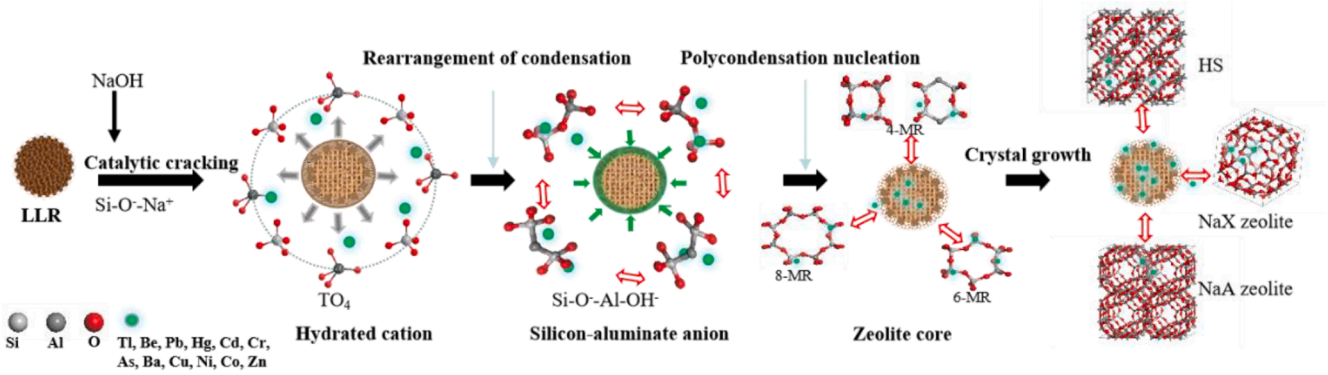

Fig. 8. Mechanism of toxic elements encapsulation during zeolite condensation growth map.

anionic form of the metal is difficult to be fixed in the lattice by the zeolite and thus prone to precipitation (Chen et al., 2023).

In our experiments, we do not use the pretreatment method of acid washing, i.e., we do not leach and filter out the toxic elements in the reaction mixture. The role of the alkaline additives is to provide enough OH^- to allow the silicon and aluminum in the lithium slag to form hydrated cations in the presence of OH^- and to be further converted into zeolite crystal nuclei, which grow around the deleterious elements (Bukhari et al., 2015). In other words, silica-aluminate anions form zeolites on the surface of these toxic elements and grow crystalline. Meanwhile, class I and II toxic elements mainly exist in free form, and the free form of harmful toxic elements are solidified in the zeolite lattice by physical adsorption as well as ion exchange, which can form insoluble minerals and realize that the toxic elements in the product are not easy to leach out at low pH (Feng et al., 2018). The mechanism is shown in Fig. 8.

4. Conclusion

Using LLR as raw material NaX zeolite, HS, and NaA zeolite were obtained at 400 °C, 500 °C and 800 °C, respectively, in the absence of stencil agent and crystal species by regulating the alkali melting temperature of two-step alkali melting method. The specific surface areas were HS > NaX > NaA zeolites, which realized a high conversion rate of > 90 % for the elements of Si and Al. The leaching test showed that the LLR leaching Be and Tl exceeded the standard limits and were hazardous wastes. In addition, Be, Ba, Cu, and Zn showed significant mobility under acidic or alkaline conditions. On the contrary, the mobility of these toxic elements in the synthesized zeolite was significantly reduced, and none of them reached the limit of hazardous wastes in leaching at pH = 3.21. During zeolite preparation, the toxic elements were immobilized in the zeolite structure, while the toxic elements contents in the zeolite cleaning wastewater all met the standard limits. The study proved that the preparation of hazardous waste LLR into zeolite is technically feasible. At the same time, from the environmental protection point of view, it not only reduces the risk of its environmental leaching, it also ensures that there will be no secondary pollution to the environment during production and product use, and realizes the resourcefulness of hazardous waste.

Funding

This work was funded by the National Key R&D Program of China [No. 2019YFC1805100], Jiangxi Provincial Natural Science Foundation [No. 20232ACB203026], the National Natural Science Foundation of China [No. 51664025], the Pingxiang Science and Technology Project [No. 2022C0102], and the Jiangxi Provincial Key Laboratory of Environmental Pollution Prevention and Control in Mining and Metallurgy [No. 2023SSY01071].

Ethics approval.

Not applicable, research does not report on or involve the use of any animal or human data or tissue.

Consent to participate.

Not applicable.

Consent for publication

The authors consent for publication of the manuscript in Arabian Journal of Chemistry (ARABJC).

CRediT authorship contribution statement

Zongli Wang: Writing – review & editing, Writing – original draft, Project administration. **Xianli Luo:** Methodology, Data curation. **Xiaojun Zheng:** Writing – review & editing. **Ming Chen:** Formal analysis. **Haifeng Guo:** Formal analysis. **Qi Li:** Data curation.

References

Aguilar-Carrillo, J., Herrera, L., Gutierrez, E.J., 2018. Solid-phase distribution and mobility of thallium in mining-metallurgical residues: environmental hazard implications. Environ. Pollut. 243, 1833–1845. https://doi.org/10.1016/j.envpol.2018.10.014.

Baldermann, A., Grießbacher, A., Baldermann, C., et al., 2018. Removal of barium, cobalt, strontium, and zinc from solution by natural and synthetic allophane adsorbents. Geosciences 8. https://doi.org/10.3390/geosciences8090309.

Baldermann, A., Fleischhacker, Y., Schmidthaler, S., et al., 2020. Removal of barium from solution by natural and iron(III) oxide-modified allophane, beidellite and zeolite adsorbents. Materials (Basel). 13 https://doi.org/10.3390/ma13112582.

Bukhari, S.S., Behin, J., Kazemian, H., et al., 2015. Conversion of coal fly ash to zeolite utilizing microwave and ultrasound energies: a review. Fuel 140, 250–266. https://doi.org/10.1016/j.fuel.2014.09.077.

Calugaru, I.L., Neculita, C.M., Genty, T., et al., 2018. Metals and metalloids treatment in contaminated neutral effluents using modified materials. J. Environ. Manage. 212, 142–159. https://doi.org/10.1016/j.jenvman.2018.02.002.

Cao, J., Wang, P., Sun, Q., 2020. Green synthesis of magnetic zeolite LTA using NaOH activated fly ash. Zeitschrift Für Anorganische Und Allgemeine Chemie. 646, 1666–1670. https://doi.org/10.1002/zaac.202000215.

Chen, D., Hu, X., Shi, L., et al., 2012. Synthesis and characterization of zeolite X from lithium slag. Appl. Clay Sci. 59–60, 148–151. https://doi.org/10.1016/j.clay.2012.02.017.

Chen, L., Yao, J., Zhang, G., 2018. Flexural properties of lithium slag concrete beams subjected to loading and thermal-cold cycles. KSCE J. Civ. Eng. 23, 624–631. https://doi.org/10.1007/s12205-018-0449-0.

Cheng, J., Hua, X., Zhang, G., et al., 2024. Synthesis of high-crystallinity Zeolite A from rare earth tailings: investigating adsorption performance on typical pollutants in rare earth mines. J Hazard Mater. 468, 133730 https://doi.org/10.1016/j.jhazmat.2024.133730.

Criado, M., Palomo, A., Fernandezjimenez, A., 2005. Alkali activation of fly ashes. Part 1: effect of curing conditions on the carbonation of the reaction products. Fuel 84, 2048–2054. https://doi.org/10.1016/j.fuel.2005.03.030.

Dong, P., Ahmad, M.R., Chen, B., et al., 2021. Preparation and study of magnesium ammonium phosphate cement from waste lithium slag. J. Clean. Prod. 316 https://doi.org/10.1016/j.jclepro.2021.128371.

Feng, W., Wan, Z., Daniels, J., et al., 2018. Synthesis of high quality zeolites from coal fly ash: mobility of hazardous elements and environmental applications. J. Clean. Prod. 202, 390–400. https://doi.org/10.1016/j.jclepro.2018.08.140.

Gordina, N.E., Borisova, T.N., Klyagina, K.S., et al., 2022. Investigation of NH3 desorption kinetics on the LTA and SOD zeolite membranes. Membranes. 12 https://doi.org/10.3390/membranes12020147.

He, Z.-H., Li, L.-Y., Du, S.-G., 2017. Mechanical properties, drying shrinkage, and creep of concrete containing lithium slag. Constr. Build. Mater. 147, 296–304. https://doi.org/10.1016/j.conbuildmat.2017.04.166.

He, Q., Si, S., Song, L., et al., 2019. Refractory petrochemical wastewater treatment by K(2)S(2)O(8) assisted photocatalysis. Saudi J. Biol. Sci. 26, 849–853. https://doi.org/10.1016/j.sjbs.2017.07.009.

Heard, C.J., Grajciar, L., Rice, C.M., et al., 2019. Fast room temperature lability of aluminosilicate zeolites. Nat Commun. 10, 4690. https://doi.org/10.1038/s41467-019-12752-y.

Huang, Y., Jin, B., Zhong, Z., et al., 2004. Trace elements (Mn, Cr, Pb, Se, Zn, Cd and Hg) in emissions from a pulverized coal boiler. Fuel Process. Technol. 86, 23–32. https://doi.org/10.1016/j.fuproc.2003.10.022.

Huang, S., Wang, Y., Zhang, L., et al., 2023. Insight into the kinetic behavior of microwave-assisted synthesis of NaX zeolite from lithium slag. New J. Chem. 47, 14335–14343. https://doi.org/10.1039/d3nj02260a.

Inoue, K., Parajuli, D., Ghimire, K.N., et al., 2017. Biosorbents for Removing Hazardous Metals and Metalloids. Materials (Basel). 10 https://doi.org/10.3390/ma10080857.

Jain, A.K., Jasra, R.V., Bhat, S.G.T., 1990. Liquid-phase adsorption of olefin/paraffin mixtures on ion-exchanged X zeolite. Sep. Sci. Technol. 25, 489–505. https://doi.org/10.1080/01496399008050345.

Jiang, Z., Yang, J., Ma, H., et al., 2015. Synthesis of pure NaA zeolites from coal fly ashes for ammonium removal from aqueous solutions. Clean Techn. Environ. Policy 18, 629–637. https://doi.org/10.1007/s10098-015-1072-0.

Kesler, S.E., Gruber, P.W., Medina, P.A., et al., 2012. Global lithium resources: relative importance of pegmatite, brine and other deposits. Ore Geol. Rev. 48, 55–69. https://doi.org/10.1016/j.oregeorev.2012.05.006.

Kim, K.-M., Oh, H.-T., Lim, S.-J., et al., 2016. Adsorption equilibria of water vapor on zeolite 3A, zeolite 13X, and dealuminated Y zeolite. J. Chem. Eng. Data 61, 1547–1554. https://doi.org/10.1021/acs.jced.5b00927.

Kuang, G., Li, H., Hu, S., et al., 2015. Recovery of aluminium and lithium from gypsum residue obtained in the process of lithium extraction from lepidolite. Hydrometall. 157, 214–218. https://doi.org/10.1016/j.hydromet.2015.08.020.

Li, J., Huang, S., 2020. Recycling of lithium slag as a green admixture for white reactive powder concrete. J. Mater. Cycles Waste Manage. 22, 1818–1827. https://doi.org/10.1007/s10163-020-01069-4.

Li, W., Jin, H., Xie, H., et al., 2023. Utilization of electrolytic manganese residue to synthesize zeolite A and zeolite X for Mn ions adsorption. J. Ind. Eng. Chem. 120, 147–158. https://doi.org/10.1016/j.jiec.2022.12.021.

Li, L., Liu, C., Ma, R., et al., 2021. Enhanced oxidative and adsorptive removal of thallium(I) using Fe3O4@TiO2 decorated RGO nanosheets as persulfate activator and adsorbent. Sep. Purif. Technol. 271 https://doi.org/10.1016/j.seppur.2021.118827.

Li, L., Xu, S., Liu, Z., et al., 2024. Insight into the growth mechanism of low-temperature synthesis of high-purity lithium slag-based zeolite A. Materials (Basel). 17 https://doi.org/10.3390/ma17030568.

Lv, Y., Ma, B., Liu, Y., et al., 2022. Adsorption behavior and mechanism of mixed heavy metal ions by zeolite adsorbent prepared from lithium leach residue. Microporous and Mesoporous Materials 329. https://doi.org/10.1016/j.micromeso.2021.111553.

Mamaghani, F.A.A., Salem, A., Salem, S., 2023. A novel technique for fabrication of rod-like shape zeolite LTA and hydroxysodalite by extrusion of bentonite powder: effects of technical factors on structural characteristics. Adv. Powder Technol. 34 https://doi.org/10.1016/j.apt.2023.104085.

Muriithi, G.N., Petrik, L.F., Doucet, F.J., 2020. Synthesis, characterisation and CO2 adsorption potential of NaA and NaX zeolites and hydrotalcite obtained from the same coal fly ash. J. CO2 Util. 36, 220–230. https://doi.org/10.1016/j.jcou.2019.11.016.

Novembre, D., di Sabatino, B., Gimeno, D., et al., 2018. Synthesis and characterization of Na-X, Na-A and Na-P zeolites and hydroxysodalite from metakaolinite. Clay Miner. 46, 339–354. https://doi.org/10.1180/claymin.2011.046.3.339.

Palomo, A., Krivenko, P., Garcia-Lodeiro, I., et al., 2014. A review on alkaline activation: new analytical perspectives. Materiales De Construcción. 64 https://doi.org/10.3989/mc.2014.00314.

Prokof'ev, V.Y., Gordina, N.E., 2014. Preparation of granulated LTA and SOD zeolites from mechanically activated mixtures of metakaolin and sodium hydroxide. Appl. Clay Sci. 101, 44–51. https://doi.org/10.1016/j.clay.2014.07.008.

Roy, T., Plante, B., Benzaazoua, M., et al., 2023. Geochemistry and mineralogy of a spodumene-pegmatite lithium ore at various mineral beneficiation stages. Miner. Eng. 202 https://doi.org/10.1016/j.mineng.2023.108312.

Senila, M., Neag, E., Cadar, O., et al., 2022. Simultaneous removal of heavy metals (Cu, Cd, Cr, Ni, Zn and Pb) from aqueous solutions using thermally treated romanian zeolitic volcanic tuff. Molecules 27. https://doi.org/10.3390/molecules27123938.

Sivalingam, S., Sen, S., 2018. Optimization of synthesis parameters and characterization of coal fly ash derived microporous zeolite X. Appl. Surf. Sci. 455, 903–910. https://doi.org/10.1016/j.apsusc.2018.05.222.

Sun, X., Hao, H., Zhao, F., et al., 2017. Tracing global lithium flow: a trade-linked material flow analysis. Resour. Conserv. Recycl. 124, 50–61. https://doi.org/10.1016/j.resconrec.2017.04.012.

Wang, Y., Ren, F.-F., Pan, D.-H., et al., 2016. A hierarchically micro-meso-macroporous zeolite CaA for methanol conversion to dimethyl ether. Crystals 6. https://doi.org/10.3390/cryst6110155.

Wei, X., Zhou, Y., Tsang, D.C.W., et al., 2020. Hyperaccumulation and transport mechanism of thallium and arsenic in brake ferns (Pteris vittata L.): a case study from mining area. J. Hazard Mater. 388, 121756 https://doi.org/10.1016/j.jhazmat.2019.121756.

Wu, Y., Lee, C.P., Mimura, H., et al., 2018. Stable solidification of silica-based ammonium molybdophosphate by allophane: application to treatment of radioactive cesium in secondary solid wastes generated from fukushima. J. Hazard Mater. 341, 46–54. https://doi.org/10.1016/j.jhazmat.2017.07.044.

Xu, Z., Zhang, Y., Pan, J., et al., 2023. In situ LA–ICP–MS analyses of muscovite: constraints on granite-type Li mineralization in northwestern Jiangxi. South China. Ore Geology Reviews. 156 https://doi.org/10.1016/j.oregeorev.2023.105402.

Yang, L., Qian, X., Yuan, P., et al., 2019. Green synthesis of zeolite 4A using fly ash fused with synergism of NaOH and Na2CO3. J. Clean. Prod. 212, 250–260. https://doi.org/10.1016/j.jclepro.2018.11.259.

Yiren, W., Dongmin, W., Yong, C., et al., 2019. Micro-morphology and phase composition of lithium slag from lithium carbonate production by sulphuric acid process. Constr. Build. Mater. 203, 304–313. https://doi.org/10.1016/j.conbuildmat.2019.01.099.

Zeng, R., Tang, W., Ding, C., et al., 2019. Preparation of anionic-cationic co-substituted hydroxyapatite for heavy metal removal: performance and mechanisms. J. Solid State Chem. 280 https://doi.org/10.1016/j.jssc.2019.120960.

Zhai, H., Bian, C., Yu, Y., et al., 2019. Sustainable route for synthesis of all-silica SOD zeolite. Crystals 9. https://doi.org/10.3390/cryst9070338.

Zhao, Z., Zhang, Y., Othman, R.M., et al., 2024. CO2 adsorption by coal fly ash zeolite and modified zeolite-templated carbon. Process Saf. Environ. Prot. 186, 151–165. https://doi.org/10.1016/j.psep.2024.03.103.

Zheng, X., Qiu, S., Zhou, B., 2024. Leaching of heavy metals from tungsten mining tailings: a case study based on static and kinetic leaching tests. Environ. Pollut. 342, 123055 https://doi.org/10.1016/j.envpol.2023.123055.